Supplementary Material for "Experimental demonstration of a magnetically induced warping transition in a topological insulator mediated by rare-earth surface dopants"

Beatriz Muñiz Cano,[†] Yago Ferreiros,[†] Pierre A. Pantaleón,[†] Ji Dai,[‡] Massimo Tallarida,[‡] Adriana I. Figueroa,[¶] Vera Marinova,[||] Kevin García-Díez,[§] Aitor Mugarza,[§] Sergio O. Valenzuela,[§] Rodolfo Miranda,[†] Julio Camarero,[†] Francisco Guinea,[†] Jose Angel Silva-Guillén,[†] and Miguel A. Valbuena[*,†]

[†]Instituto Madrileño de Estudios Avanzados, IMDEA Nanociencia, Calle Faraday 9, 28049, Madrid, Spain

[‡]ALBA Synchrotron Light Source, 08290, Cerdanyola del Vallès, Barcelona, Spain

[¶]Departament de Física de la Matèria Condensada, Universitat de Barcelona, 08028 Barcelona, Spain.

[§]Catalan Institute of Nanoscience and Nanotechnology (ICN2), CSIC and BIST, Campus UAB, 08193, Barcelona, Spain

[||]Institute of Optical Materials and Technologies, Bulgarian Academy of Sciences, Acad. G. Bontchev, Str. 109, 1113, Sofia, Bulgaria

[⊥]ICREA Institució Catalana de Recerca i Estudis Avançats, Lluis Companys 23, 08010, Barcelona, Spain

[#]Departamento de Física de la Materia Condensada; Instituto "Nicolás Cabrera" and Condensed Matter Physics Center (IFIMAC), Universidad Autónoma de Madrid (UAM), Campus de Cantoblanco, 28049, Madrid, Spain

[@]Donostia International Physics Center, Paseo Manuel de Lardizábal 4, 20018, San Sebastián, Spain; and Ikerbasque, Basque Foundation for Science, 48009, Bilbao, Spain

E-mail: miguelangel.valbuena@imdea.org

I. Growth methods

Single crystals of Bi_2Se_2Te were obtained by a modified Bridgman method in a standard crystal growth system. Powdered high purity Bi (99.999%), Se (99.999%) and Te (99.999%) were used as starting materials. The same were annealed at a temperature of 200°C in a vacuum of 10^{-4} torr for 24 hours to release water vapor since these materials in powder form are hygroscopic. The starting materials were placed in a quartz ampoule with a diameter of 20 mm, which had previously been cleaned and annealed for 8 hours at 1100°C in a vacuum of 10^{-5} torr. The ampoule was placed in the Bridgman crystal growth apparatus and the temperature was gradual and uniformly raised up to 880°C during 3 days and held at this temperature for 2 days and then cooled to 670°C at a rate of 0.5°C/hour and further cooled to room temperature at a rate of 10°C/hour. A coarse-crystalline ingot was obtained, with monocrystalline areas of typical dimensions of 5 x 3 x 0.1 mm^3.

The samples were characterized by X-ray powder diffraction (XRD) and Raman spectroscopy. XRD patterns were collected within the range from 10 to 80° 2Θ with a constant step 0.02° 2Θ on a Bruker D8 Advance diffractometer with Cu Kα radiation and LynxEye detector. Phase identification was performed with the Diffracplus EVA using the ICDD-PDF2 Database. The Raman spectra were measured in backscattering geometry in the range of 150-500 cm^{-1} in a HORIBA Jobin Yvon Labram HR visible spectrometer (Horiba Ltd., Kyoto, Japan) equipped with a Peltier-cooled CCD detector. The 632.8 nm line of a He-Ne laser was used for the excitation.

II. Er deposition and X-ray photoemission spectroscopy (XPS) coverage calibration

Rare-earths (RE) were sublimated from an e-beam evaporator and deposited on a freshly cleaved Bi_2Se_2Te surface. Previously and in order to avoid oxide deposition, the RE were outgassed for more than 24 hours. The Er coverage of the samples was calculated using the Beer-Lambert law,[1,2] which describes the attenuation of radiation passing through a material, applied to XPS experiments. In this estimation, which assumes a homogeneous Er layer of thickness d on top of an infinitely thick and homogeneous Bi_2Se_2Te substrate, the photoemitted electron intensity (I_0) is reduced when trespassing the heterostructure resulting in a transmitted intensity (I_t) given by:[3]

$$I_t = I_0 \cdot e^{-d/\lambda} \rightarrow d = -\lambda \cdot ln(I_t/I_0), \tag{1}$$

where λ is the inelastic mean free path of a photoemitted electron from a solid for a certain energy, which can be calculated as:[4]

$$\lambda(E) = \frac{143}{E^2} + 0.054\sqrt{E} \tag{2}$$

Bi 5d peaks were used for the estimations since they represent intense features in Bi_2Se_2Te. The Bi 5d peak spectra were normalized, Shirley-background substracted and multipeak fitted. $I_{t,0}$ are obtained by integrating the area below the Bi 5d peak. In our experiments I_0 = $I_{pristine}$ and $I_t = I_{Er}$ and λ (68.3 eV) = λ (71.4 eV) $\sim$ 0.480 nm, calculated from eq. 2, or λ (68.3 eV) = λ (71.4 eV) $\sim$ 0.479 nm, extracted from NIST database,[5] as the energy used for the XPS experiments was 100 eV and Bi 5d peaks binding energies are 26.9 and 23.8 eV and the analyzer work function is 4.8 eV. For the calculation of the thickness of one single monolayer we consider the Er layer to be formed following an hcp distribution of the atoms with c_{Er} = 0.559 nm so, as a result of the hcp structure, the interlayer separation is 1 ML = $c_{Er}/2$ = 0.280 nm. In Fig. S1 we provide some representative multipeak fitted XPS spectra used for the estimation of the intensities, which yield to Er coverages of 0.077 nm =

0.27 ML $\sim$ 0.3 ML (deposition time: 20 s), 0.156 nm = 0.56 ML $\sim$ 0.6 ML (40 s) and 0.254 nm = 0.92 ML $\sim$ 0.9 ML (60 s), whose ratios ($d_{40s}/d_{20s} = 2.24 \sim 2$, $d_{60s}/d_{20s} = 3.35 \sim 3$, $d_{60s}/d_{40s} = 1.61 \sim 1.5$) are also in agreement with the *in-situ* estimated amount of deposited Er with a quartz crystal microbalance.
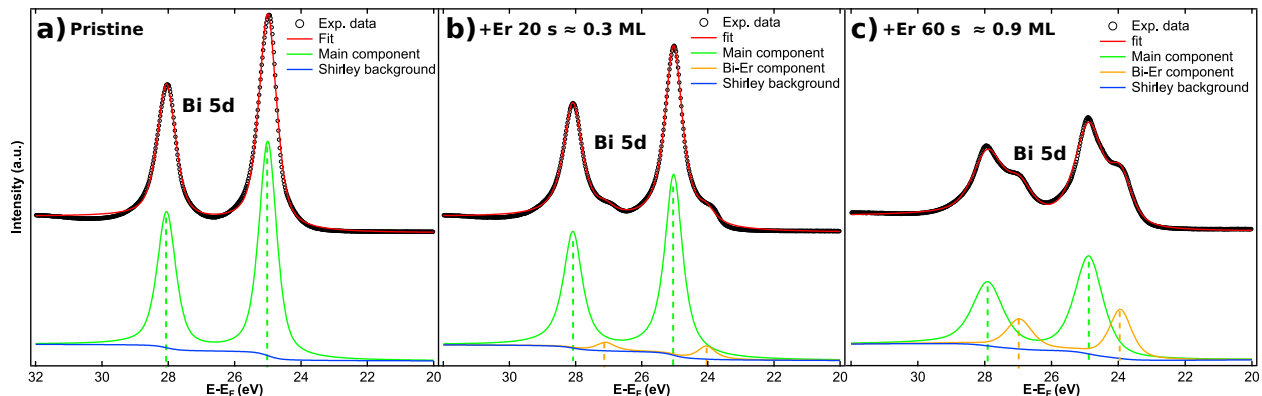

Fig. S1: Multipeak fit of XPS data acquired with hν = 100 eV for (a) pristine sample, (b) 0.3 ML Er-doped sample (20 s deposition) and (c) 0.9 ML Er-doped sample (60 s deposition). The analysis yields to coverages of 0.15 ML (10 s), 0.3 ML (20 s), 0.6 ML (40 s) and 0.9 ML (60 s). An energy shift can be appreciated following the dashed lines, consistent with a charge transfer between Er and the substrate.

III. Er/Bi$_2$Se$_2$Te extended ARPES and XPS data

In the following some complementary data for the main text, including Bi$_2$Se$_2$Te and Bi$_2$Se$_2$Te-Er doped ARPES valence band (VB) maps (Fig. S2), their X-ray photoemission spectroscopy (XPS) characterizations (Fig. S3) and the highest Bi$_2$Se$_2$Te Er-doped coverage (0.9 ML) ARPES characterization (Fig. S4).
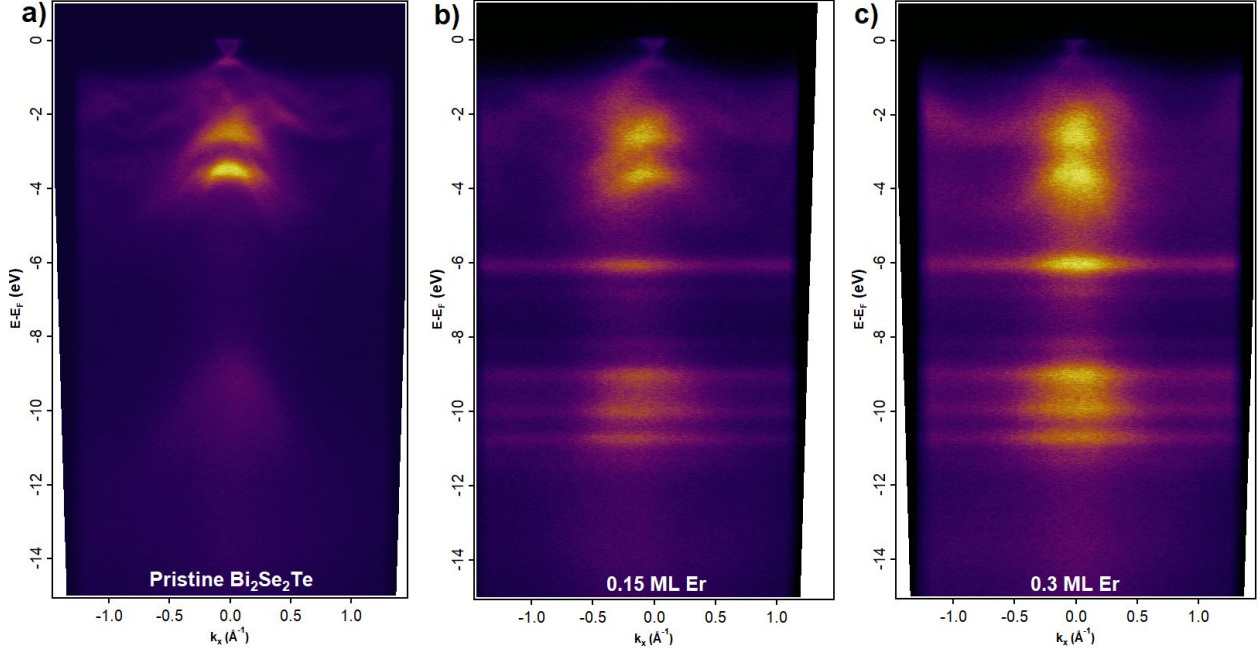

Fig. S2: ARPES VB maps along $\overline{\Gamma K}$ for (a) pristine Bi$_2$Se$_2$Te, (b) 0.15 Er ML and (c) 0.3 Er ML showing no further effects apart from the consistent attenuation of the Bi$_2$Se$_2$Te states and the emergence of 4f Er localized states as a consequence of Er deposition.
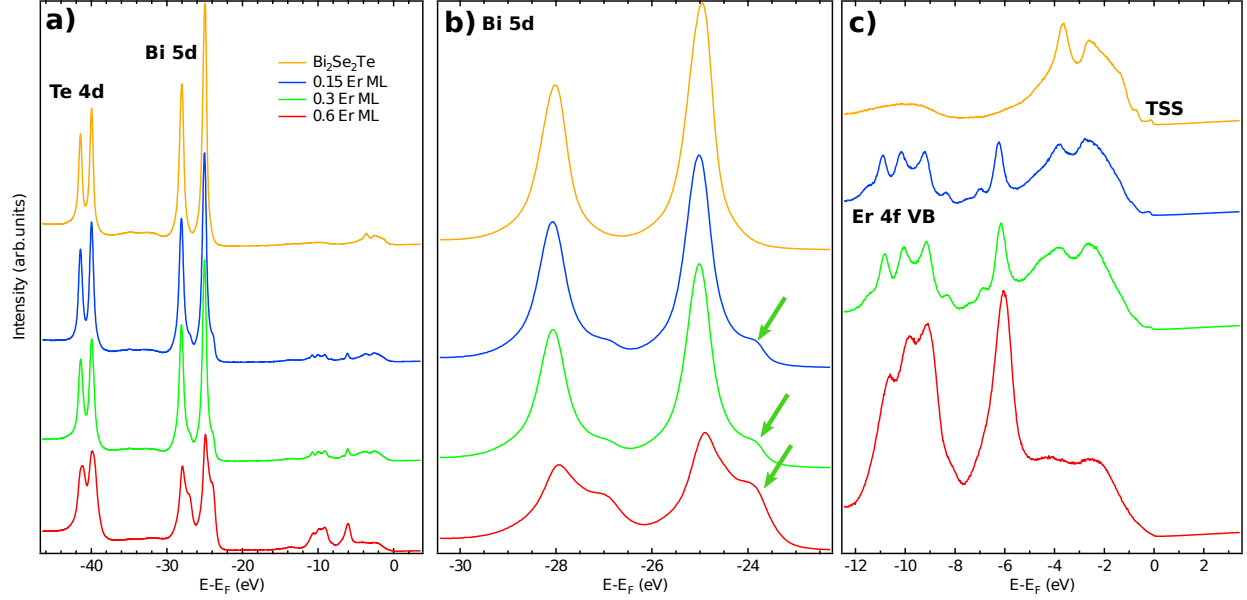
Fig. S3: XPS spectra at normal emission acquired with $h\nu = 100$ eV at T = 15 K for pristine Bi_2Se_2Te and different Er-doped Bi_2Se_2Te preparations showing (a) the complete VB, (b) the Bi 5d peak, revealing the emergence of a second Bi 5d component at lower BE (green arrows) whose intensity increases linearly with the Er coverage, and (c) the closer region to the E_F, where the Bi_2Se_2Te TSS can be observed and Er 4f VB states emerge and become more prominent as the deposited Er amount is increased.

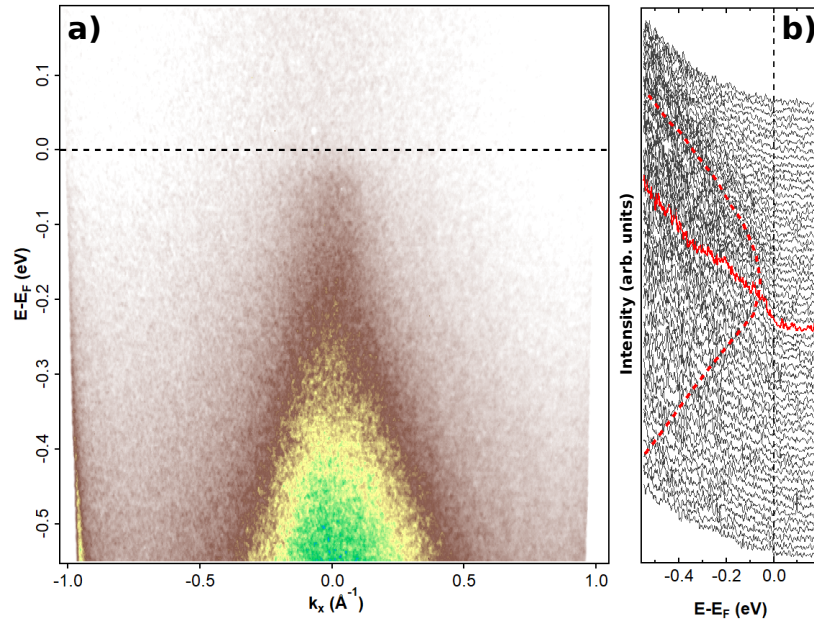Fig. S4: (a) TSS band map and (b) EDCs extracted from TSS band map for 0.9 Er ML-doped Bi_2Se_2Te. TSS dispersion is indicated in (b) with a red dashed. Solid red line highlight the EDC at $\overline{\Gamma}$. After further p-doping induced by deposition of Er impurities the DP can be located at the Fermi level.

IV. Dy/Bi$_2$Se$_2$Te extended ARPES and XPS data

Additonal XPS and ARPES characterization in Dy (0.3 ML) / Bi$_2$Se$_2$Te (Fig. S5 and Fig. S6), is presented. Very similar effects are observed after Dy deposition as the described in the main text for Er magnetic impurties. A similar development of an extra component at the Bi 5d core level is observed in XPS measurements, and more importantly, the same hexagonal to trigonal transition at the warped TSS is also observed by ARPES.
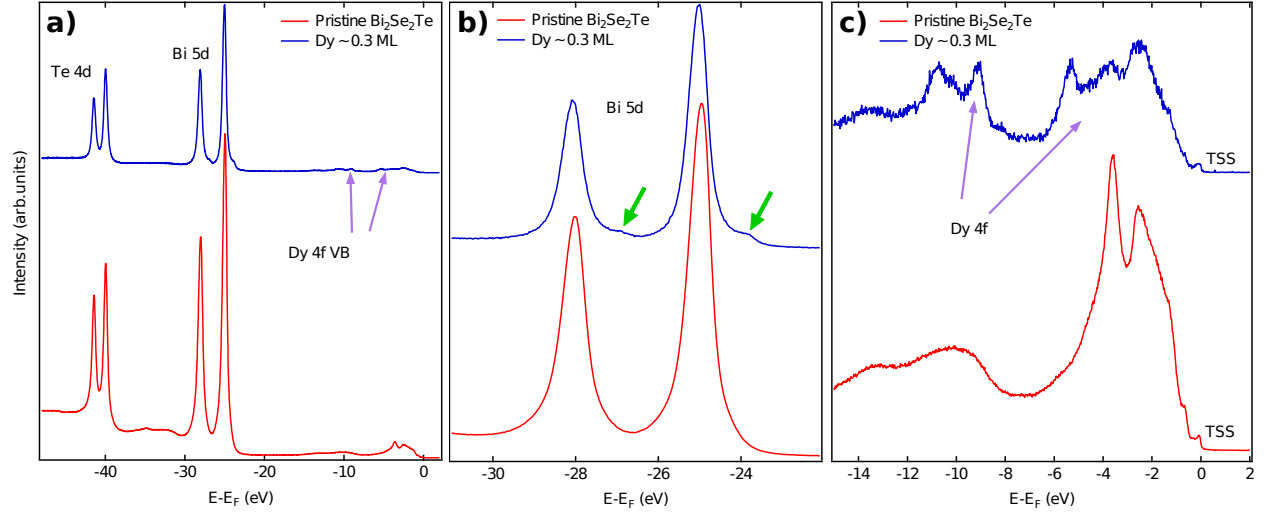

Fig. S5: XPS spectra at normal emission acquired with hν = 100 eV at T = 15 K for pristine Bi$_2$Se$_2$Te and Dy-doped Bi$_2$Se$_2$Te showing the same energy ranges as in Fig. S3.

An analogous analysis of the XPS spectra as the one performed in Fig. S1 has been performed to calculate the amount of evaporated Dy which, considering a hcp structure with c_{Dy} = 0.565 nm, yields to 0.3 Dy ML.
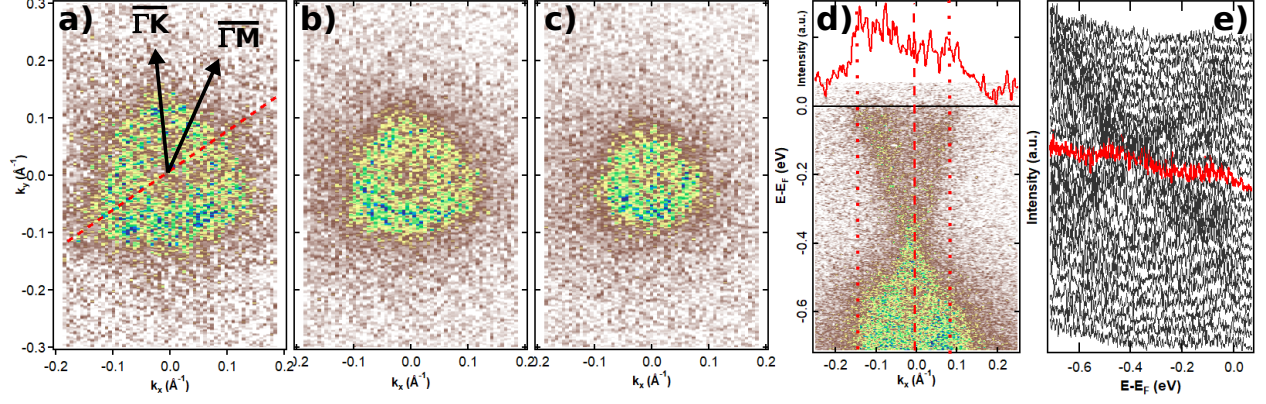
Fig. S6: (a)-(c) FS and CE maps at 100 and 200 meV below E_F for 0.3 Dy ML doped Bi_2Se_2Te showing the trigonal warping of the TSS. (d) TSS ARPES band maps along red dashed line in (a) and its MDC extracted at E_F show how the induction of a trigonal warping in the TSS is also evidenced by the k_F asymmetry around Γ. (e) EDCs extracted from (d) showing the assymetry of the two dispersive branches of the TSS, consistent with the hexagonal-to-trigonal transition. A broadening in the vicinity of the DP, similar as what was observed in the Er-doped system, is indicative of a possible gap opening. Doping effects seems to be less pronounced than in Er doped systems.

V. Theoretical model

The Hamiltonian for the surface states of the TI was derived by Fu:[6]

$$H = \hbar v(k_x \sigma_y - k_y \sigma_x) + \frac{\lambda}{2}(k_+^3 + k_-^3)\sigma_z, \tag{3}$$

with $k_\pm = k_x \pm ik_y$. The last term is only invariant under threefold rotation and is responsible for the hexagonal warping. Eq. (3) can be written as:

$$H = \hbar v(k_x \sigma_y - k_y \sigma_x) + \frac{\lambda}{2}k^3 \cos 3\theta \sigma_z, \tag{4}$$

with θ the azimuth angle of momentum: $k_\pm = k(\cos\theta \pm i\sin\theta)$. The dispersion relation reads:

$$E^2 = \hbar^2 v^2 k^2 + \lambda^2 k^6 \cos^2 3\theta. \tag{5}$$

The sixfold symmetry under $\theta \to \theta + 2\pi/6$ is apparent here.

Now we dope the surface of the TI with magnetic impurities, with out-of-plane magnetization $\boldsymbol{M} = S\gamma/a^3\boldsymbol{m}$, where S is the spin and γ is the gyromagnetic ratio of the magnetic impurities, a^3 is the volume occupied by each spin, and $\boldsymbol{m} = \boldsymbol{z}$ is the unit magnetization vector, which points in the out-of-plane ($\boldsymbol{z}$) direction. We assume a ferromagnetic Zeeman-type coupling to the surface electrons of the TI, which we can model by an exchange coupling Δ as $-\Delta\boldsymbol{m} \cdot \boldsymbol{\sigma} = -\Delta\sigma_z$. The Hamiltonian takes the form:[7]

$$H = \hbar v(k_x \sigma_y - k_y \sigma_x) + (\lambda k^3 \cos 3\theta - \Delta)\sigma_z, \tag{6}$$

The dispersion relation reads now:

$$E^2 = \hbar^2 v^2 k^2 + (\lambda k^3 \cos 3\theta - \Delta)^2. \tag{7}$$

See that, because of time reversal breaking due to the magnetic impurities, now there is a term which is linear in $\cos 3\theta$. Therefore the symmetry has reduced to threefold under $\theta \to \theta + 2\pi/3$.

As for the fitting of the exchange coupling coefficient Δ, in Fig. S7 we provide the lower

limit where the experimental FS and CE maps were moderately well fitted by the theoretical model, that is, the value in which the trigonal symmetry becomes slightly visible, in such a way that the difference between the optimized Δ value, of 0.12 eV, and the aforementioned limit could give an idea on the accuracy of the estimation of such a parameter.
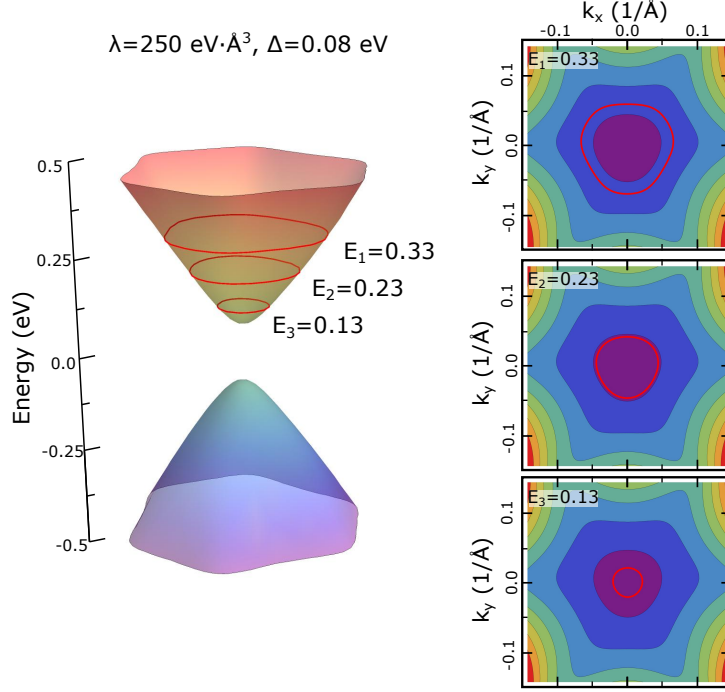

Fig. S7: **Lowest Δ value for which the theoretical constant energy (CE) contours start to develop an incipient trigonal shape**. Band structure of the surface state of a topological insulator and the evolution of the CE maps (red lines) as a function of the Fermi energy for the system with magnetic impurities, with $\Delta = 0.08$ eV. The very initial transition from a hexagonal to a trigonal warping, as well as the induction of a gap, start to become visible. The panels in the right display CE maps at three different energies relative to the Dirac point, corresponding to the energies of the experimental ones. As compared to the reported value in the main text, of 0.12, the accuracy of the theoretical model can be inferred.

Moreover, we have observed how the effective transition from a hexagonal to a trigonal warping takes place unequivocally (in Fig. S7 we show the extremal value for Δ in which the trigonal shape begins to be slightly distinguished) in the range from $\Delta = 0.1$ eV and $\Delta = 0.12$ eV, being the former the value for which the experimentally observed trigonal warping is perfectly reproduced by the model.

VI. Theoretical prove of the Fermi velocity anisotropy upon Er doping

In the absence of RE dopants, the Fermi velocity (v_F) of the system, of $7.1 \cdot 10^5$ m/s as extracted from the experimental data, exhibits symmetry with respect to the center of the Dirac cone, i.e., the Γ point (see Fig. 3(g) in the main text). As the v_F is an input for the theoretical model, the same effect is observed in Fig. S8(b), which is the momentum vs. energy dispersion obtained along the black line in the Fermi surface map in Fig. S8(a). However, upon the addition of RE dopants, the hexagonal band structure transforms into a trigonal one, as explained in the main text, as a consequence of which a change in the average v_F is observed (see Fig. 3(h)). This effect is also developed in the theoretical model where, with the only incorporation of the Zeeman-like term in the hamiltonian describing the pristine system (whose inputs included the aforementioned unique v_F value, of $7.1 \cdot 10^5$ m/s, which is never modified), an anisotropy in the v_F is observed. As in the pristine sample, we extract a momentum vs. energy dispersion from the orange line in Fig. S8(c), shown in Fig. S8(d). Furthermore, by fitting a line to the theoretical gapped cone shown in Fig. S8(d) we determine that the slopes of the two branches are different. Specifically, in the same momentum interval, the slopes of the lines are $8.2 \cdot 10^5$ m/s and $9.8 \cdot 10^5$ m/s for the red and blue lines, respectively, which aligns with our experimental findings, of $(8.0 \pm 0.3) \cdot 10^5$ and $(1.2 \pm 0.1) \cdot 10^6$ m/s for the branches corresponding to the vertex and the flat face of the trigonal TSS, respectively. Thus, our observations indicate that the branches of the gapped Dirac cone possess distinct average Fermi velocities due to the trigonal symmetry of the energy bands, a phenomenon verified both experimental and theoretically.
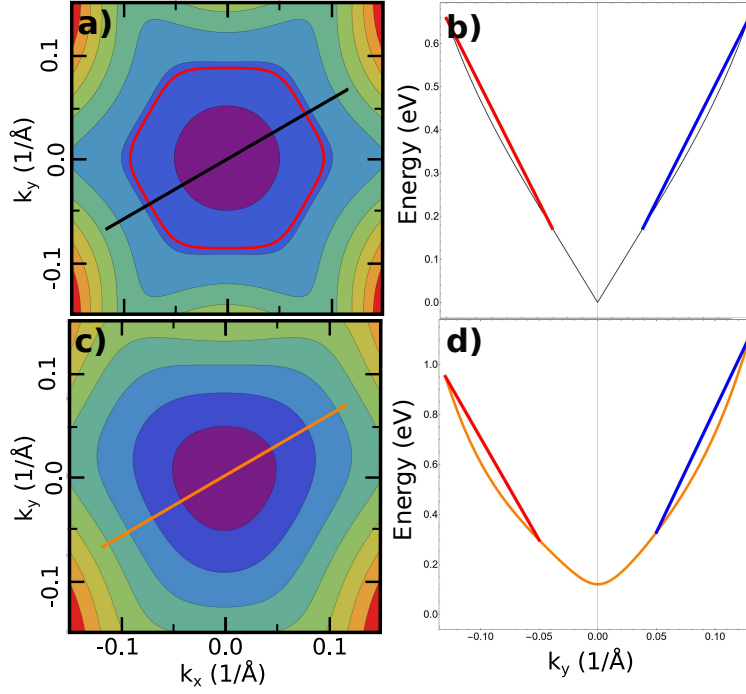
Fig. S8: (a, c) Fermi surface maps and (b, d) momentum vs. energy dispersions extracted from the black and orange lines (which display variations in the distance between consecutive constant energy lines) in (a, c) for the theoretically modelled pristine (a, b) and magnetically doped (c, d) samples, reproducing the experimentally observed anisotropy in the Fermi velocity.

VII. MDCs and EDCs fittings: band dispersion and gap opening

In order to get the accurate band dispersion of the TSS for the pristine and Er-doped Bi_2Se_2Te systems, curvature and second derivative procedures have been applied to the raw ARPES bandmaps, which are shown in Figs. S9. As clearly observed in the second derivative maps, the punctual DP in the pristine sample evolves to a sizeable intensity broadening, consistent with an energy gap opening.
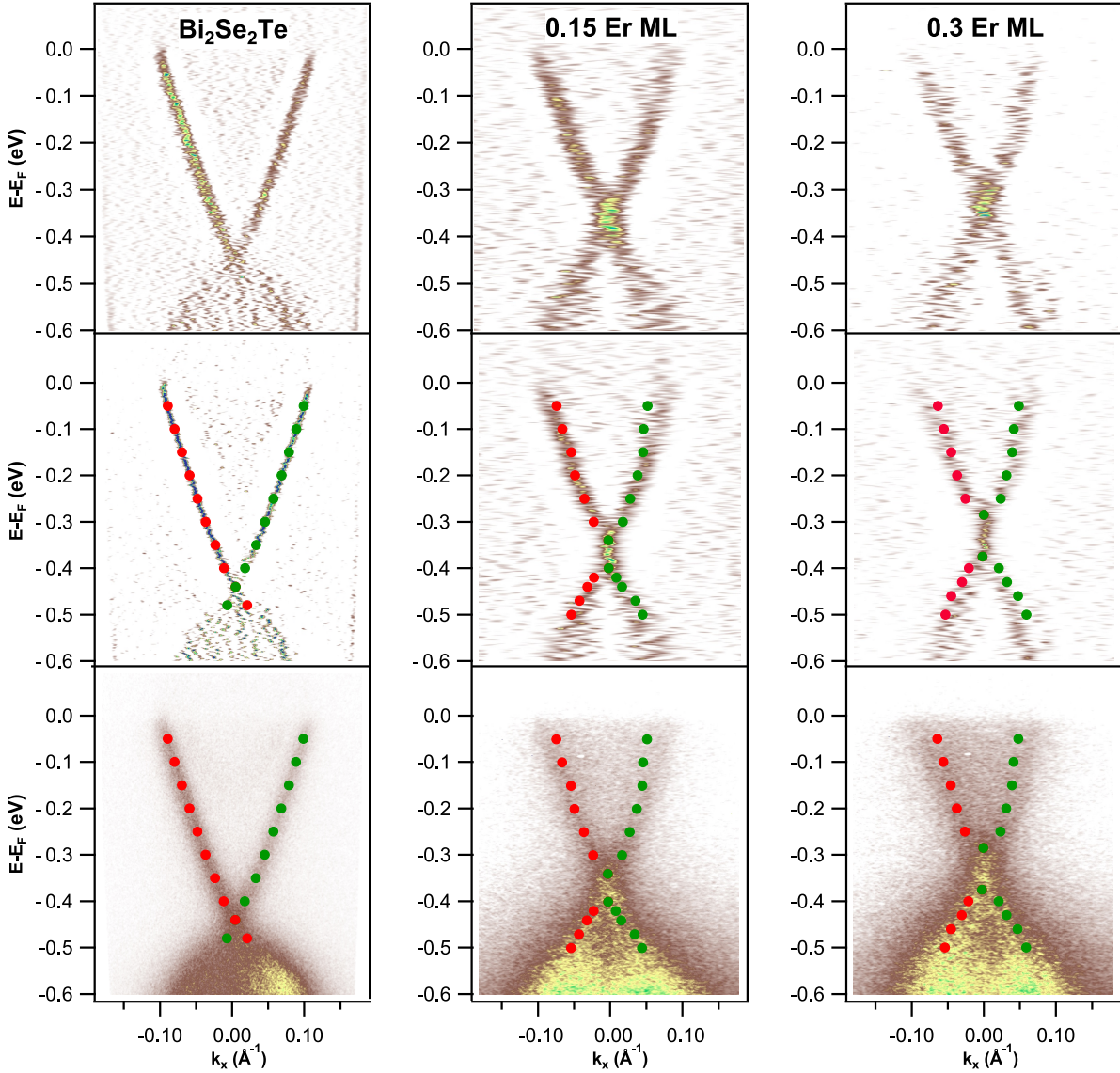

Fig. S9: Upper row: Second derivative (intensity vs. momentum) of the ARPES bandmaps shown in Fig. 5 of the main text. Middle row: same as upper row with the MDC fitting results obtained in Fig. S10 (red and green dots) superimposed. Bottom row: raw ARPES band maps merged with the MDC fitting results (Fig. S10).
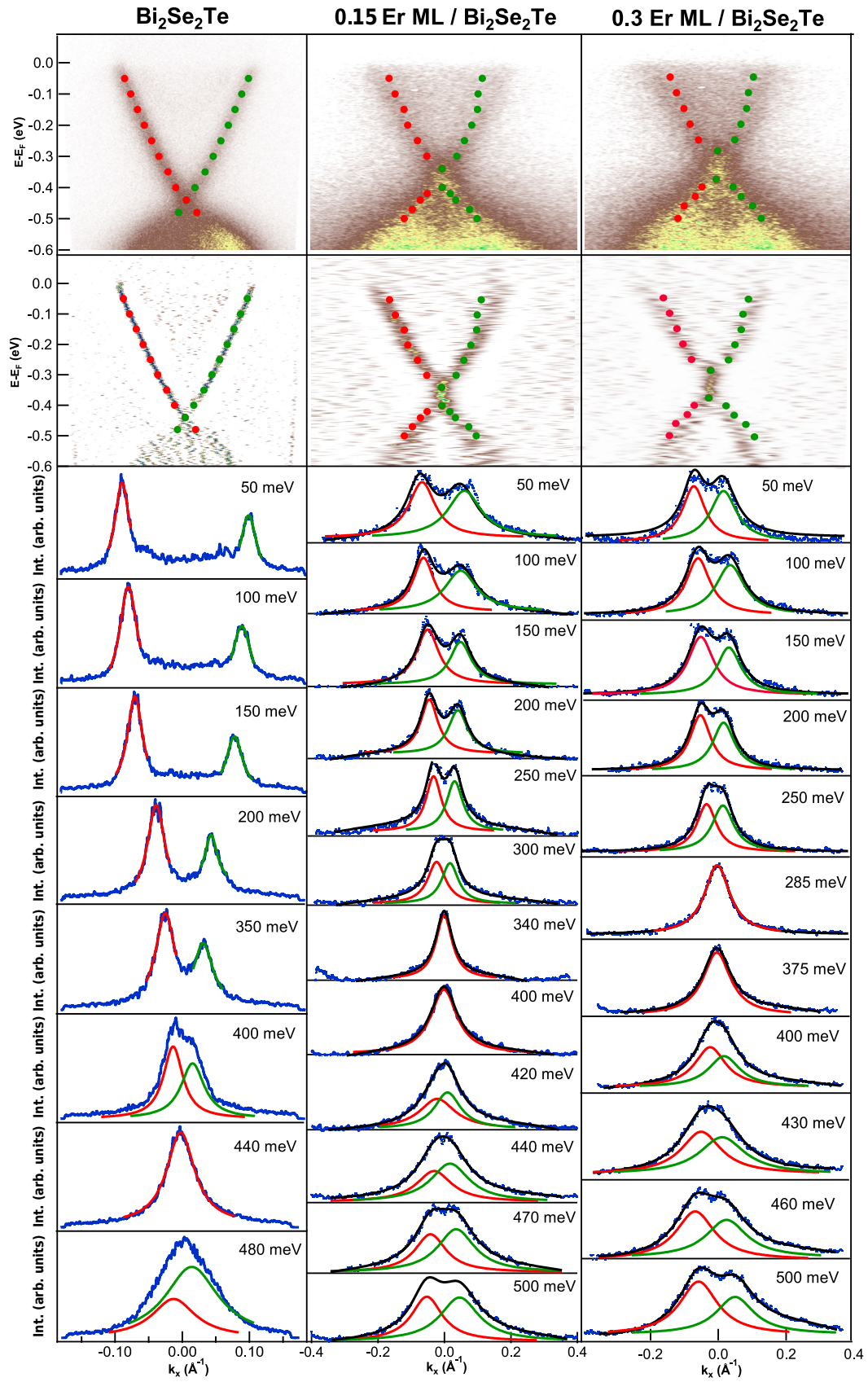
Fig. S10: Summary of the MDCs fitting results.

The band dispersion has been directly gathered from the MDCs fitting results (Fig. S10). A *Wavemetrics Igor Pro* multi-peak fitting procedure was used to fit the MDCs for the pristine and the 0.15 and 0.30 ML Er-doped systems. The fitted MDCs are presented in Fig. S10, whose peaks were fitted to lorentzian functions. It is important to highlight that in the broadened energy region (the one around the DP) for the 0.15 and 0.3 ML Er-doped samples, the corresponding MDCs can only be fitted with a single lorentzian peak, showing no dispersion in this energy region and consistent with the interpretation of a band gap opening. By preserving the color correspondence with respect to the peaks (red and green curves) that constitute the fitted curve of each MDC (bottom panels), red and green dots at the corresponding energy vs. momentum positions are superimposed on the ARPES and the second derivative maps (top panels) in Fig. S10 (also in Fig. S9). Moreover, these results are also consistent with the EDC fittings, as shown in Fig. S11, Fig. S12, and the comparison between the MDCs and EDCs fitting results in Fig. S13.

The color-highlighted EDCs in Fig. 5 in the main text correspond to those at the Γ point, whose fitting results for pristine and 0.15 and 0.3 ML Er-doped samples are shown in Fig. S11. Another home-made *Wavemetrics Igor Pro* procedure was used to fit the EDCs, which takes into account the Fermi edge step and its broadening with the temperature, as well as a Shirley background. The peaks were fitted to Voigt functions, whose fitting parameters consider their amplitude, width, energy position and line-shape (which can be gradually tuned from pure gaussian to pure loretnzian functions and all intermediate values). The EDC crossing the DP for the pristine sample can only be fitted to a single peak (red peak in Fig. S11(a)), in addition to a large contribution coming from bulk bands (blue peak). When the Er doping is introduced, the previously described energy broadening is explained by the double peak necessary to fit the EDCs at Γ, consistent with the band gap opening between the surface state bottom band (red peaks in Figs. S11(c) and (e)), and the top of bulk valence band (green peaks in Figs. S11(c) and (e)).
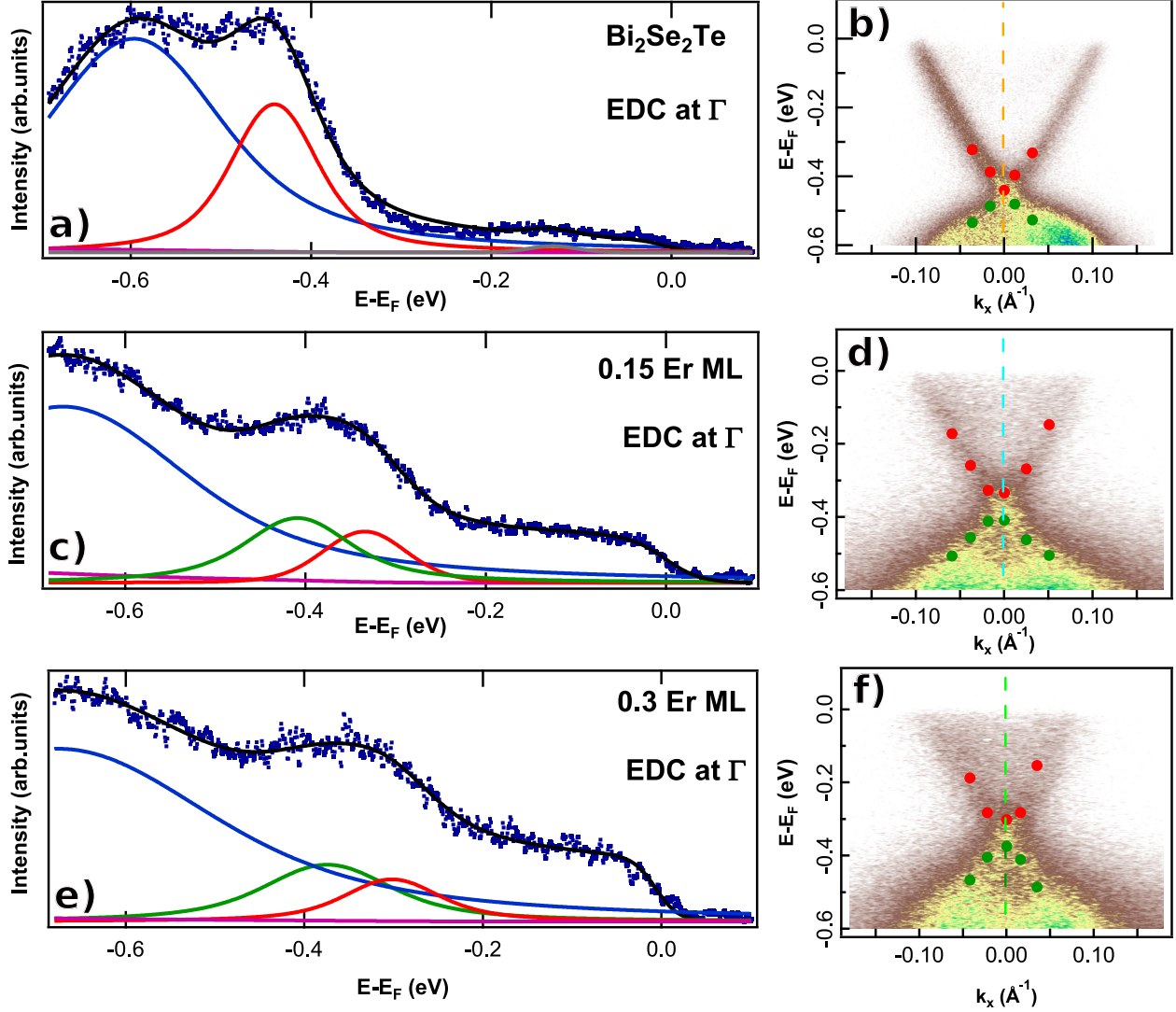
14

Fig. S11: EDCs at Γ. Fitting results for pristine (a, b) and 0.15 (c, d) and 0.3 (e, f) ML Er-doped Bi$_2$Se$_2$Te. Two peaks (green and red curves) are necessary to fit the DP at Γ for the Er-doped systems, while only one is required for the pristine one. Dark blue dots correspond to raw data; the solid black line to the fitting result; and the blue, green, red and grey peaks are the contributions from the bulk valence band, the top of valence band, the surface state bottom and the conduction bulk band gap, respectively. The background contribution is not shown for simplicity.

The energies obtained for the maxima of the fitted red and blue peaks are approximately -0.33 eV and -0.41 eV (0.15 Er ML, Fig. S11(c) and (d)), and -0.30 and -0.37 eV (0.3 Er ML, Figs. S11(e) and (f)), respectively. These results are consistent with the MDC fits, which revealed an energy broadening region around the DP (where MDCs are better fit to a single peak) ranging from -0.34 to -0.40 eV (0.15 Er ML, Fig. S10, middle column) and from -0.285

to -0.375 eV (0.3 Er ML, Fig. S10, right column). Based on these results, from the MDC end EDC fits, the gap amplitude can be estimated to be of ~ 70 meV for both systems, and the p-type doping already analyzed in the main text is further proved.
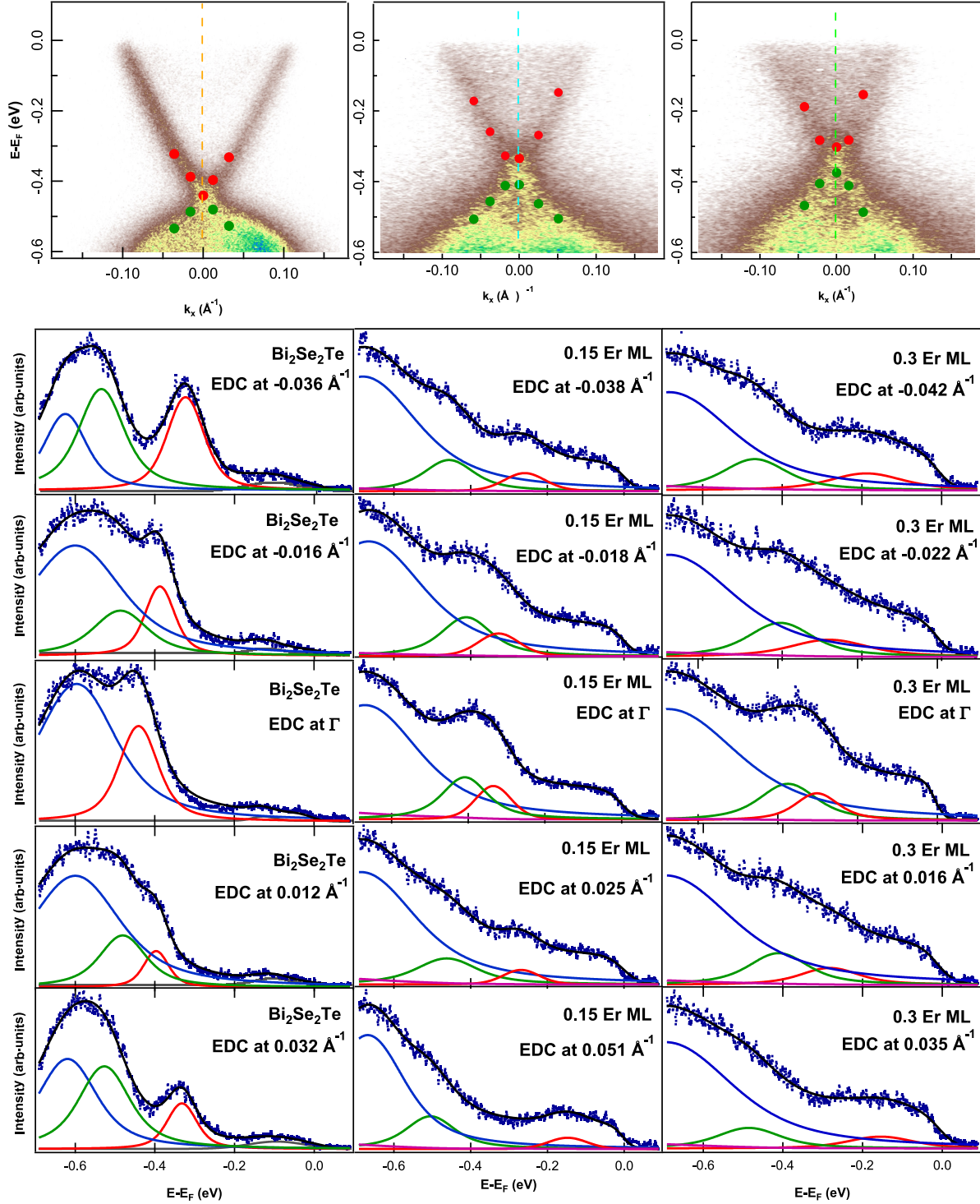

Fig. S12: Summary of EDCs fitting results.

A summary of the EDC fits is shown in Fig. S12. Note than an extra tiny peak (in grey) in the flat region close to the Fermi level has been added in order to take into account the conduction bulk band and to properly fit the EDCs of the pristine system.
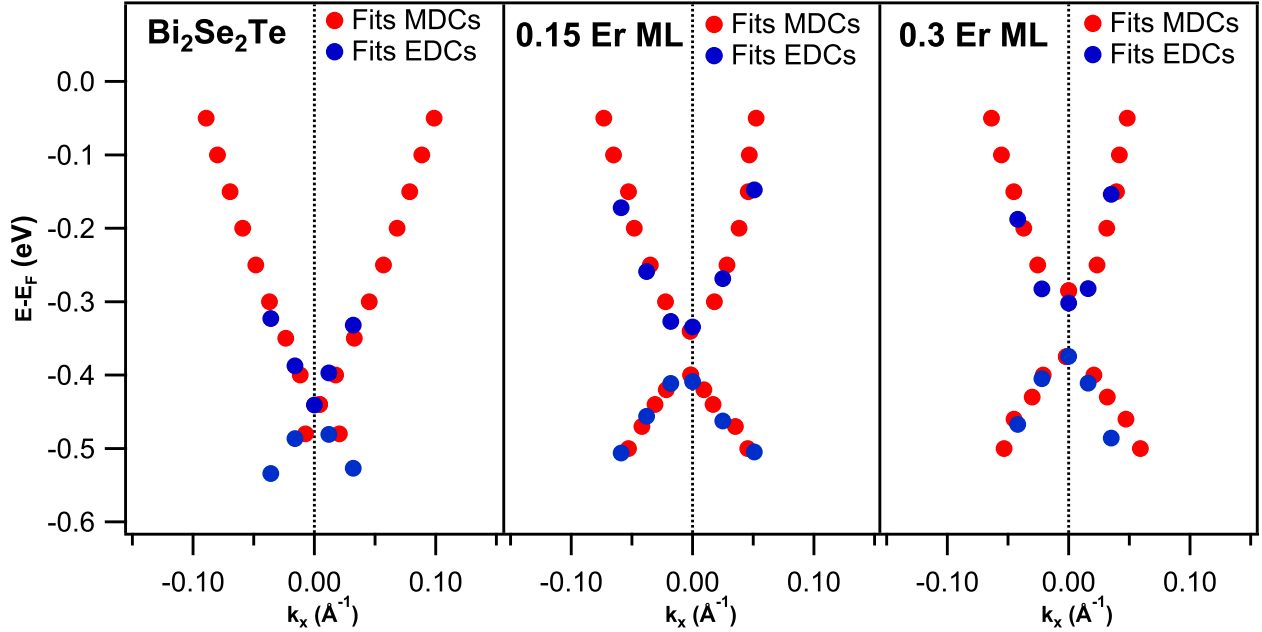

Fig. S13: Comparison of MDC (Figs. S9 and S10) and EDC (Figs. S11 and S12) fitting results.

Finally, in order to corroborate the consistency between the MDC and EDC fits, their are merged in Fig. S13, with an excellent agreement between them, illustrating both the band asymmetry and the gap opening.

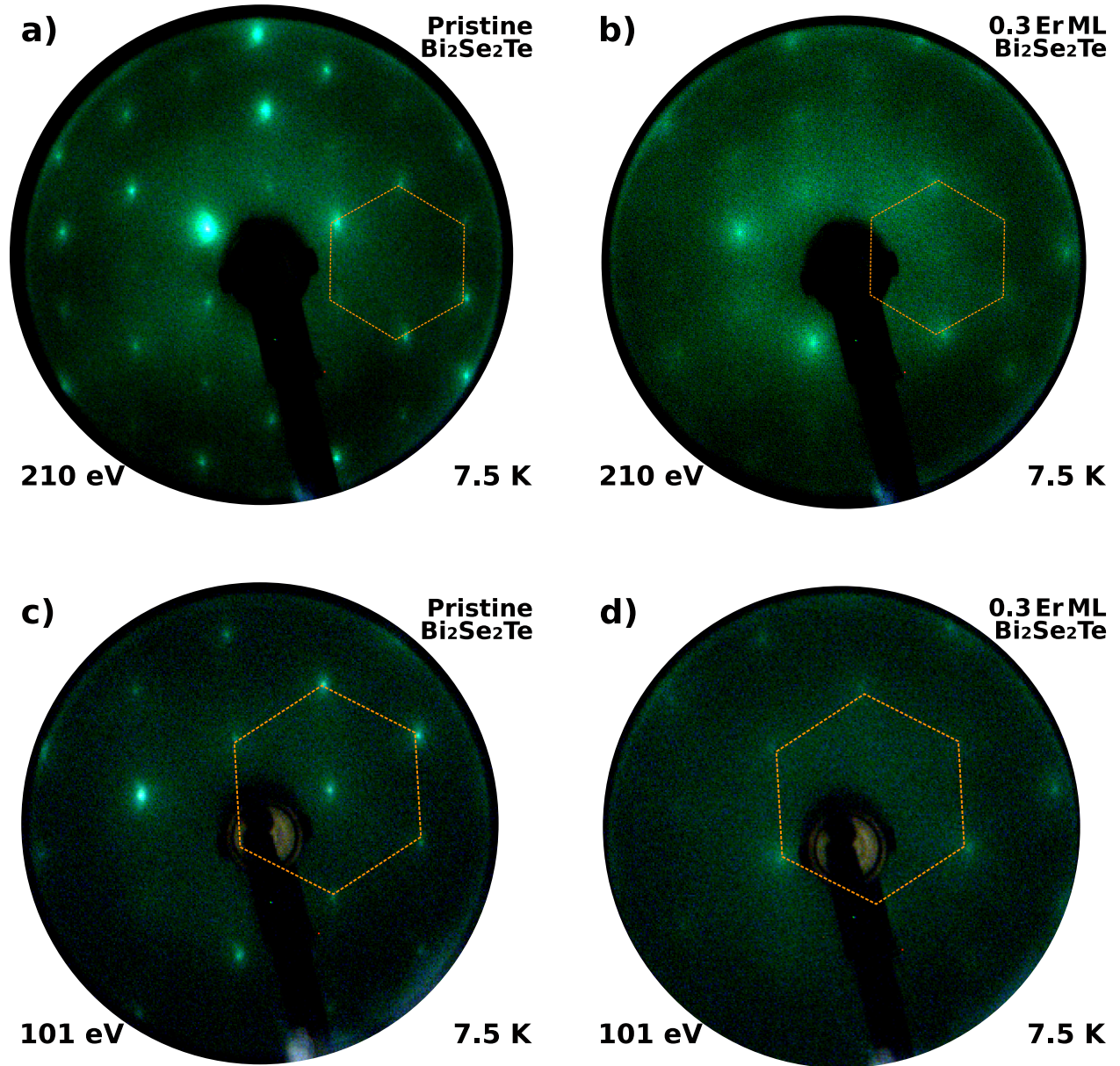# VIII. Structural characterization: LEED patters

Fig. S14: LEED patterns of the pristine (left, (a) and (c)) and 0.3 Er doped (right, (b) and (d)) samples acquired at 210 (top, (a) and (b)) and 110 eV (bottom, (c) and (d)) at the same temperature as the ARPES experiment (15 K) not showing any kind of additional crystalline order or surface reconstruction (as indicated by the dashed hexagon).

References

(1) Beer, A. Bestimmung der absorption des rothen lichts in farbigen flussigkeiten. *Annalen der Physik* **1852**, *162*, 78–88.

(2) Lambert, J.-H. *Photometria, sive de Mensura et gradibus luminis, colorum et umbrae*; sumptibus viduae E. Klett, 1760.

(3) Mayerhöfer, T. G.; Pahlow, S.; Popp, J. The Bouguer-Beer-Lambert law: Shining light on the obscure. *ChemPhysChem* **2020**, *21*, 2029–2046.

(4) Seah, M. P.; Dench, W. Quantitative electron spectroscopy of surfaces: A standard data base for electron inelastic mean free paths in solids. *Surface and interface analysis* **1979**, *1*, 2–11.

(5) Powell, C. J.; Jablonski, A. NIST Electron Inelastic-Mean-Free-Path Database. *National Institute of Standards and Technology (NIST) Chemistry WebBook* **2010**, data retrieved from NIST Standard Reference Database 71, `https://www.nist.gov/srd/nist-standard-reference-database-71`.

(6) Fu, L. Hexagonal warping effects in the surface states of the topological insulator Bi 2 Te 3. *Physical Review Letters* **2009**, *103*, 266801.

(7) Naselli, G.; Moghaddam, A. G.; Di Napoli, S.; Vildosola, V.; Fulga, I. C.; van den Brink, J.; Facio, J. I. Magnetic warping in topological insulators. *Physical Review Research* **2022**, *4*, 033198.